Random singlet-like state in the dimer-based triangular antiferromagnet $Ba_6Y_2Rh_2Ti_2O_{17-\delta}$

Wonjun Lee [1], Sungwon Yoon [2], Sungmin Jeon [2], Yipeng Cai [3], Kenji Kojima [3,4], Loi T. Nguyen [5], R. J. Cava [5], Kwang-Yong Choi [2,*] and Suheon Lee [1,†]

[1] *Center for Artificial Low Dimensional Electronic Systems, Institute for Basic Science, Pohang 37673, Republic of Korea*
[2] *Department of Physics, Sungkyunkwan University, Suwon 16419, Republic of Korea*
[3] *TRIUMF, 4004 Wesbrook Mall, Vancouver, British Columbia, Canada V6T 2A3*
[4] *Stewart Blusson Quantum Matter Institute, University of British Columbia, Vancouver, British Columbia, Canada V6T 1Z4*
[5] *Department of Chemistry, Princeton University, Princeton, New Jersey 08544, USA*

(Received 30 October 2023; accepted 10 May 2024; published 3 June 2024)

We present the magnetic, thermodynamic, and muon spin relaxation (μSR) results of the dimer-based triangular antiferromagnet $Ba_6Y_2Rh_2Ti_2O_{17-\delta}$. The magnetic susceptibility data show the sub-Curie-Weiss behavior $\chi(T) \propto T^{-\alpha_\chi}$ below 100 K, suggesting random magnetism. The isothermal magnetization results reveal the presence of weakly interacting structural orphan spins about 6.1% at 2 K, arising from the oxygen deficiency. The comprehensive μSR experiments exhibit the coexisting relaxing and nonrelaxing components along with the thermally activated behavior in the muon spin relaxation rate, reflecting the fluctuating orphan spins in the dimer singlet background. In addition, we observe the scaling behavior of $M(H,T)$ in H/T and $P_z(t)$ in t/H_{LF} with the scaling exponents $\alpha_\chi = \alpha_{\mathrm{M}} = 0.75$ and $\alpha_\mu = 0.72$, respectively, but not for the magnetic specific heat data. The failure of the scaling relation in $C_{\mathrm{m}}(H,T)/T$ implies low-energy excitations dressed by the conventional orphan spins. Based on these observations, we find that the magnetic ground state resembles random singlets and discuss the possible configurations of the spin dimer unit Rh_2O_9. Our results shed light on the role of quenched disorder in the dimer-based frustrated magnets.

DOI: 10.1103/PhysRevResearch.6.023225

I. INTRODUCTION

Spin-dimer systems have gathered great theoretical and experimental interest due to novel low-energy phenomena and a crossover from three-dimensional to zero-dimensional magnetism [1–3]. It is well known that antiferromagnetic intradimer interactions give rise to either a spin-singlet or a spin-triplet ground state in the absence of further couplings. However, in the presence of interdimer interactions, the system can host long-range magnetic order depending on the relative energy scale of the interdimer interaction J_{inter} and the singlet-triplet excitation energy Δ [3]. When $J_{\mathrm{inter}} < \Delta$, the singlet-triplet excitation acquires a finite bandwidth. On the other hand, for $J_{\mathrm{inter}} > \Delta$, long-range magnetic order can be driven by mixing different states.

Singularly, the dimer singlet serves as a fundamental building block for a range of exotic quantum states of matter due to entangled spin pairs. In dimer-based systems, the regular arrangement of singlet pairs leads to a valence bond solid [4,5]. On the other hand, when spins form a superposition of multiple singlet configurations, either a dynamic valence bond or a resonating valence bond can be realized [6,7]. Furthermore, if there is disorder or exchange randomness among singlets, the system hosts an unconventional random-singlet state [9]. In this vein, the dimer singlet is widely employed to realize exotic quantum states, such as a valence bond glass and a quantum spin liquid (QSL) [7,8].

As one of the long-sought quantum states, QSL has been intensively explored in the last decades, in which the system evades long-range magnetic order down to 0 K due to quantum fluctuations [7]. In real materials, the presence of intrinsic disorder hinders the formation of true QSLs. Instead, it is suggested that quenched disorder can promote a quantum-disordered or a random-singlet state [9–14]. For instance, in $YbMgGaO_4$, the cation mixing between Mg^{2+} and Ga^{3+} leads to orientational spin disorder, mimicking QSL behavior [15]. In $H_3LiIr_2O_6$, the bond disorder or vacancy gives rise to the coexisting random singlets and disordered Kitaev spin liquid with exotic low-energy magnetic excitations [16–19]. Lastly, $Sr_2CuTe_{1-x}W_xO_6$ displays gapless QSL behavior for $x = 0.5$ [20] and a random-singlet-like state for $x = 0.05 - 0.1$ [21], driven by exchange randomness.

In particular, the random-singlet state has been regarded as the randomness-induced QSL, composed of hierarchically arranged spin singlets, resonating spin-dimer clusters, and orphan spins, with no characteristic energy scale except for the exchange coupling J [14]. Such a ground state is featured by (i) a linear T dependence of the specific heat, (ii) a gapless magnetic susceptibility with a Curie-tail at low T, and (iii) broad features of dynamic spin structure factor. In addition, remarkably, the orphan spins are not localized but can

*choisky99@skku.edu
†suheonlee@ibs.re.kr

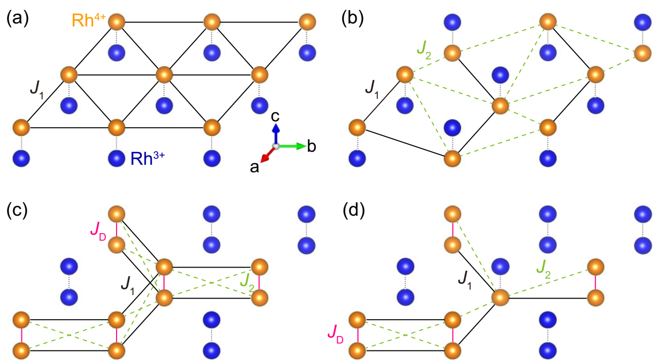

FIG. 1. Possible configurations of the Rh_2O_9 dimers in the *ab* plane. The oxygen atoms are omitted for clarity. (a) Uniformly and (b) nonuniformly distributed Rh^{4+} and Rh^{3+} ions within the Rh_2O_9 units. (c) Formally distributed $Rh_2^{4+}O_9$ and $Rh_2^{3+}O_9$ dimers. (d) Randomly distributed $Rh_2^{4+}O_9$, $Rh_2^{3+}O_9$, and $Rh^{3+}Rh^{4+}O_9$ dimers. The black solid, green dashed, pink solid lines represent the inter- and intradimer interactions J_1, J_2, and J_D, respectively.

near-freely diffuse to neighboring sites through low-energy excitations, which is the breakdown of spin singlets into two spins and their recombination with nearby spin singlets. As such, the mobile orphan spins in the random-singlet state apparently differ from the conventional (structural) orphan spins, which originate from structural imperfection and are immobile in the system. However, both types of orphan spins provide similar experimental signatures, making it difficult to distinguish between them.

Recently, the dimer-based triangular antiferromagnet $Ba_6Y_2Rh_2Ti_2O_{17-\delta}$ has been proposed to be a QSL candidate material with quenched disorder [22]. $Ba_6Y_2Rh_2Ti_2O_{17-\delta}$ crystallizes in the hexagonal structure (space group No. 194 $P6_3/mmc$) [22]. In this compound, Rh_2O_9 dimers form a triangular layer in the *ab* plane with the interdimer distance 5.94 Å via the super-super-exchange interactions with the pathway Rh-O-O-Rh, which are widely separated (∼14.76 Å) by nonmagnetic YO_6 octahedra and TiO_4 tetrahedra. Notably, the system has intrinsic oxygen deficiency $\delta = 0.57$ at the O4 site, located in the middle layer of three Ba slabs between the triangular planes [22].

Such oxygen deficiency leads to the 1:1 mixed valence character of Rh^{4+} and Rh^{3+}, resulting in three different dimer units in the system: a spin dimer $Rh_2^{4+}O_9$, nonmagnetic $Rh_2^{3+}O_9$, and orphan-spin-like $Rh^{4+}Rh^{3+}O_9$. Depending on their population in the system, four distinct spin topologies are expected as illustrated in Fig. 1. First, the uniformly positioned Rh^{4+} and Rh^{3+} ions within the dimer unit form a uniform triangular lattice in the *ab*-plane with the exchange coupling J_1 [Fig. 1(a)]. Second, the nonuniformly distributed Rh^{4+} and Rh^{3+} moments within Rh_2O_9 lead to a distorted triangular layer with two exchange interactions J_1 and J_2 [Fig. 1(b)]. Third, when two Rh^{4+} (Rh^{3+}) ions reside in the single dimer, the magnetic ($Rh_2^{4+}O_9$) and nonmagnetic ($Rh_2^{3+}O_9$) dimers give rise to a dimer-based depleted triangular lattice with three difference exchange couplings: the intradimer interaction J_D and interdimer interactions J_1 and J_2 [Fig. 1(c)]. Lastly, when Rh^{4+} and Rh^{3+} are randomly distributed, the system hosts random magnetism due to the cation disorder and competing interactions between J_1, J_2, and J_D [Fig. 1(d)]. However, the exact dimer configuration in $Ba_6Y_2Rh_2Ti_2O_{17-\delta}$ is far from clear.

The previous characterizations have revealed the absence of long-range order down to 0.3 K and the scaling behavior of the total specific heat in T/H with the exponent of $\alpha_C = 0.5$ [22], similar to other QSL candidate materials [23–25]. Nevertheless, the precise ground state and inherent spin dynamics in $Ba_6Y_2Rh_2Ti_2O_{17-\delta}$ remain elusive due to the lack of information about the spin dimer unit, warranting further investigations.

In this work, we revisit the magnetic and thermodynamic properties in conjunction with muon spin relaxation experiments. The magnetic characterization results suggest random magnetism with weakly interacting structural orphan spins at low temperatures. The μSR data evidence the coexistence of fluctuating conventional orphan spins and dimer singlets. Noticeably, the scaling relation is observed in the magnetic susceptibility, isothermal magnetization, and muon spin polarization data but not in the magnetic specific heat results. These observations indicate the random-singlet-like state in the dimer-based triangular antiferromagnet $Ba_6Y_2Rh_2Ti_2O_{17-\delta}$.

II. EXPERIMENTAL DETAILS

Polycrystalline specimens of $Ba_6Y_2Rh_2Ti_2O_{17-\delta}$ were synthesized using solid-state reaction as described in Ref. [22]. The sample quality was confirmed by powder x-ray diffraction, and the oxygen deficiency was determined by thermogravimetric analysis and determined to be $\delta \sim 0.57$ [22].

The magnetic properties were characterized using a Physical Property Measurement System (Quantum Design PPMS) equipped with a vibrating sample magnetometer in the temperature range of $T = 2$–100 K and the magnetic field range of $\mu_0H = 0$–9 T. The specific heat measurements were performed by the thermal-relaxation method using the PPMS with a ^{3}He insert in the temperature range of $T = 0.35$–20 K. The lattice specific heat was subtracted by the nonmagnetic counterpart $Ba_6Y_2Ti_4O_{17}$ from the total specific heat [22].

Muon spin relaxation (μSR) experiments were carried out with the LAMPF spectrometer on the M20 beamline and with the DR spectrometer on the M15 beamline at TRIUMF (Vancouver, Canada) for the temperature ranges of $T = 2$–200 and 0.03–8 K, respectively. The obtained μSR data were analyzed using the software package MUSRFIT [26]. We plotted the muon spin polarization in zero and longitudinal fields by normalizing the asymmetry using the theoretical fitting values in order to match the data acquired from the two different spectrometers.

III. RESULTS

A. Magnetic properties

Figure 2(a) shows the dc magnetic susceptibility as a function of temperature at $\mu_0H = 0.5$ T. $\chi(T)$ manifests a strong increment at low temperatures with no signature of long-range magnetic order down to 2 K. A steep enhancement of $\chi(T)$ at low T is due to the presence of orphan spins. After subtracting the orphan spin susceptibility χ_{orp}, we obtain the intrinsic

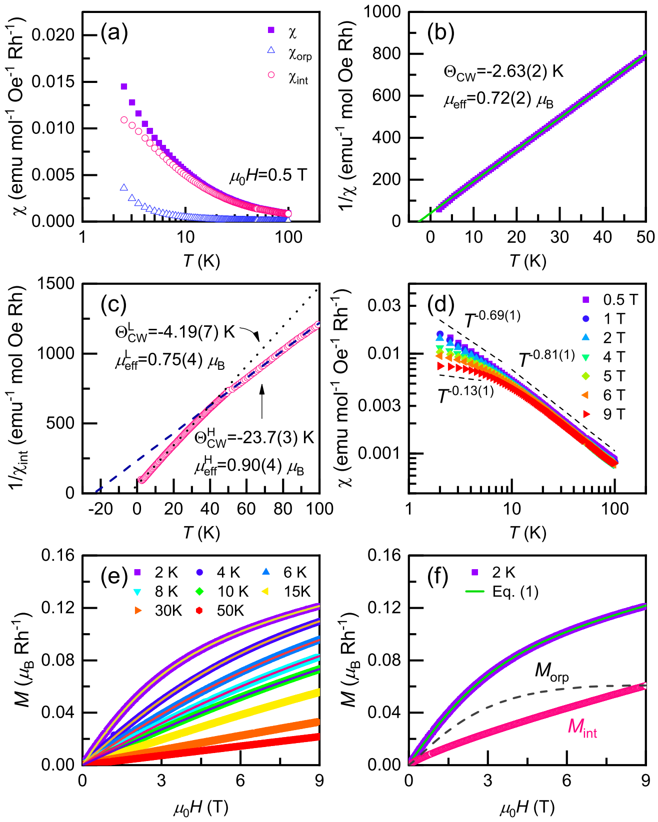

FIG. 2. (a) Temperature dependence of the dc magnetic susceptibility $\chi(T)$ at $\mu_0 H = 0.5$ T. $\chi(T)$ is decomposed into the orphan spin susceptibility $\chi_{\text{orp}}(T)$ and the intrinsic spin susceptibility $\chi_{\text{int}}(T)$. (b) Inverse magnetic susceptibility as a function of temperature. The solid line denotes the Curie-Weiss fit. (c) Temperature dependence of the inverse intrinsic magnetic susceptibility. The dashed and dotted lines represent the Curie-Weiss fits for high and low T, respectively. (d) χ vs. T in a log-log scale. The dashed lines indicate the power-law dependence $\chi(T) \sim T^{-\alpha_\chi}$. (e) Temperature dependence of the isothermal magnetization. The solid curves represent the fittings to the data using Eq. (1). (f) Isothermal magnetization at 2 K along with the fits using Eq. (1) and its decomposition into the intrinsic $M_{\text{int}}(H)$ and the orphan spin magnetization $M_{\text{orp}}(H)$.

magnetic susceptibility χ_{int}. In estimating χ_{orp}, we use the orphan spin concentration extracted from the isothermal magnetization at 2 K (see below). Upon cooling, $\chi_{\text{int}}(T)$ exhibits the curvature change through 4 K and seems to saturate to a constant value below 2 K.

As illustrated by the green line in Fig. 2(b), the Curie-Weiss law well reproduces $\chi(T)$ in the temperature range of $T =$ 10–50 K. From the fittings, we obtain the Curie constant $C = 0.0661(1)$ emu mol^{-1} Oe^{-1} K, the Weiss temperature $\Theta_{\text{CW}} = -2.63(2)$ K, and the temperature-independent constant $\chi_0 = 0.000193(2)$ emu mol^{-1} Oe^{-1}. The effective magnetic moment is evaluated to be $\mu_{\text{eff}} = 0.72(2)\ \mu_{\text{B}}$, slightly smaller than the expected value $(1.732/2 = 0.866\,\mu_{\text{B}})$ for the 1:1 mixed valence character of Rh^{4+} and Rh^{3+} in the limit of negligible covalent bonding between them. It is noteworthy that, unlike 3d transition metal ions, the itinerancy of the Ru 4d electrons can lead to the further reduction of magnetic moments. The negative value of Θ_{CW} indicates predominant antiferromagnetic interactions between the Rh ions. Using $k_{\text{B}}\Theta_{\text{CW}} = 2zS(S+1)J/3$ with $z = 6$ the nearest-neighbor coordination number of the triangular lattice, the exchange coupling constant is calculated to be $J = -0.87$ K, suggesting weak antiferromagnetic interactions between the Rh moments. Note that χ_0 is attributed to the paramagnetic moments of barium, titanium, and yttrium elements.

To gain further insight, we closely inspect $\chi_{\text{int}}(T)$. As displayed in Fig. 2(c), the inverse intrinsic susceptibility presents two distinct Curie-Weiss regimes above and below 40 K. The Curie-Weiss fits yield $C^{\text{H}} = 0.1013(3)$ emu mol^{-1} Oe^{-1} $\cdot$ K, $\Theta^{\text{H}}_{\text{CW}} = -23.7(3)$ K, and $\mu^{\text{H}}_{\text{eff}} = 0.90(4)\ \mu_{\text{B}}$ for $50 < T < 100$ K and $C^{\text{L}} = 0.0705(2)$ emu mol^{-1} Oe^{-1} K, $\Theta^{\text{L}}_{\text{CW}} = -4.19(7)$ K, and $\mu^{\text{L}}_{\text{eff}} = 0.75(4)\ \mu_{\text{B}}$ for $2 < T < 40$ K. The temperature-varying Curie-Weiss temperature implies the onset of additional exchange couplings at low temperatures. The reduction of μ_{eff} around 40 K is reminiscent of the formation of the spin singlets with decreasing temperature.

Figure 2(d) shows the temperature dependence of the dc magnetic susceptibility in various fields in a log-log scale. Above 10 K, $\chi(T)$ is field-independent, while below 10 K, $\chi(T)$ is gradually suppressed with increasing field. Remarkably, we find two different power-law regimes above and below 10 K. $\chi(T)$ follows the power-law dependence $T^{-\alpha_\chi}$ with $\alpha_\chi = 0.81(1)$ for $T > 10$ K and its exponent decreases to $\alpha_\chi = 0.13(1) - 0.69(1)$ for $T < 10$ K with varying applied field. The transition to a stronger sub-Curie behavior upon cooling through 10 K implies the build-up of abundant low-energy states, reflecting the change of spin-spin correlations. The observed high-T weak sub-Curie behavior is widely reported in the systems with random magnetism or competing exchange interactions [27–30]. It is theoretically established that quenched disorder can induce a random-singlet state with the distribution of exchange interactions $P(J) \sim J^{-\alpha_\chi}$ [9]. At a finite temperature $T > J$, the spins with J behave as free spins, leading to the power-law behavior of the dc magnetic susceptibility. Therefore, for disordered magnets by quenched disorder, the dc magnetic susceptibility is given by the sum of the power-law and the Curie-Weiss terms $\chi(T) \sim T^{-\alpha_\chi} + C/T$. In line with the theoretical prediction, $\chi(T)$ is well decomposed into $\chi_{\text{int}} \sim T^{-\alpha_\chi}$ and $\chi_{\text{orp}} \sim C/T$ as shown in Fig. 2(a), signifying the presence of quenched disorder in the system.

We turn to the isothermal magnetization data plotted in Fig. 2(e). In the high-T paramagnetic phase, $M(H)$ increases linearly up to 9 T, not following a Brillouin function. This implies that some portion of antiferromagnetically coupled spins are present even in the paramagnetic state. Below 10 K, $M(H)$ deviates from linearity while showing a Brillouin-like behavior at low fields and a linear increment at high fields. Thus we attempt to decompose the isothermal magnetization into the orphan and intrinsic spin contributions. As displayed in Figs. 2(e) and 2(f), $M(H)$ for $2 \leqslant T \leqslant 10$ K is well described with the sum of the modified Brillouin function and the power-law term given by

$$M(H) = \frac{n_{\text{orp}} g \mu_{\text{B}}}{2} \tanh\left[\frac{g\mu_{\text{B}}\mu_0 H}{k_{\text{B}}(T - T^*)}\right] + A(\mu_0 H)^n. \quad (1)$$

Here, n_{orp} is the number of the orphan spin, g is the g factor, μ_{B} is the Bohr magneton, k_{B} is the Boltzmann constant, and

TABLE I. Parameters obtained from the isothermal magnetization with Eq. (1).

T (K)	n_{orp}/N (%)	T^* (K)	n
2	6.16(1)	−0.23(1)	0.821(1)
4	5.96(3)	−0.33(1)	0.922(1)
6	4.97(2)	−1.41(1)	0.963(1)
8	3.96(6)	−2.79(5)	0.978(1)
10	3.41(4)	−4.10(3)	0.983(1)

T^* is the interaction energy scale between the orphan spins. For the fittings, we employ the typical g factor ($g = 2$) for the Rh^{4+} ($S = 1/2$) ions in the octahedral environment [31]. The extracted parameters are tabulated in Table I. In the following, we only consider the 2 K data where the orphan spin contribution is pronounced. The exponent $n = 0.821(1)$ is comparable to the exponent α_χ from $\chi(T)$ above 10 K. The slight deviation from the linear dependence alludes to the distribution of antiferromagnetic exchange interactions. The orphan spin concentration is estimated to be 6.1% from the relation of n_{orp}/N, where N is the Avogadro number. The coupling strength of $T^* = -0.237(5)$ K suggests weak antiferromagnetic interactions between the orphan spins. After subtracting the orphan spin contribution, the intrinsic magnetization increases sublinearly up to 9 T, as expected for predominant antiferromagnetic interactions [Fig. 2(f)]. Note that, as the temperature is raised, T^* gradually increases, n approaches 1, and n_{orp}/N decreases. This is because the orphan spin contribution is suppressed with increasing temperature, while the antiferromagnetic contribution becomes dominant.

Along with the sub-Curie behavior of $\chi(T)$, the sublinear dependence of $M(T)$ has been reported in a range of frustrated magnets, including the hole-doped Haldane system $Y_{2-x}Ca_xBaNiO_5$, the triangular spin ladder $KCu_5V_3O_{13}$, and the triangular antiferromagnet $Ba_3CuSb_2O_9$ [32–34]. These materials are featured by the random-singlet state or exchange randomness. Based on our magnetic characterizations, we infer that the oxygen deficiency generates the ∼6% conventional orphan spins, giving rise to the random-singlet state and/or the ground state with competing interactions.

B. μSR

In order to reveal the nature of the magnetic ground state and associated spin dynamics, we performed transverse field (TF), zero field (ZF), and longitudinal field (LF) μSR measurements. Figure 3 shows the TF-μSR data at different temperatures. We observe no loss of initial asymmetry or rapid relaxation due to static local fields, indicating the absence of long-range magnetic order down to 20 mK. The TF-μSR spectra are well described with $P_z(t) = P_z(0)\cos(2\pi f_\mu t + \phi)\exp(-\lambda_{\mathrm{TF}}t)$. Here, $P_z(0)$ is the initial asymmetry at $t = 0$, f_μ is the frequency of the muon Larmor precession by the applied TF, ϕ is the initial oscillation phase, and λ_{TF} is the muon spin relaxation rate. With decreasing temperature, λ_{TF} slightly increases and becomes nearly temperature-independent below 10 K at which $\chi(T)$ shows a change in its sub-Curie behavior [see Fig. 2(d)].

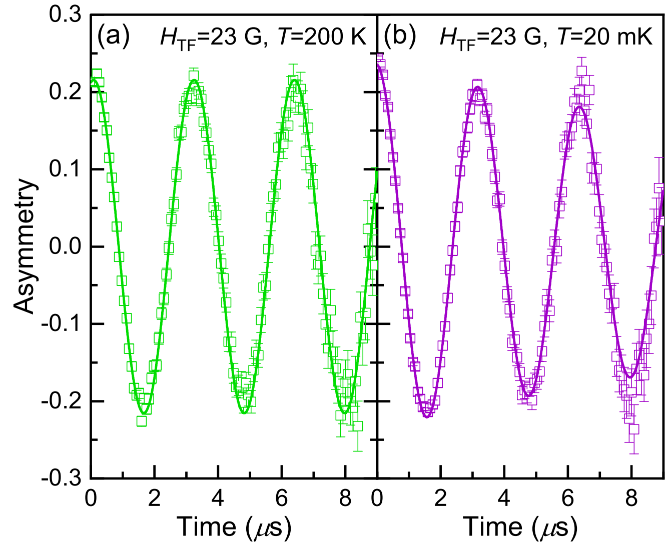

FIG. 3. Raw TF-μSR spectra at (a) $T = 200$ K and (b) 20 mK in the applied TF of $H_{\mathrm{TF}} = 23$ G. The solid curves denote the fits to the data.

Before proceeding further, it is worth noting that the raw TF spectra exhibit the initial asymmetry of ∼0.21–0.23. This suggests that the slow muon spin depolarization in the μSR data is the total muon spin relaxation in the time window of a continuous muon beam, not a 1/3 tail of the muon spin depolarization.

Figure 4(a) displays the ZF-μSR results. At higher temperatures, the polarization exhibits substantially weak relaxation, indicative of rapidly fluctuating moments by thermal energy. With decreasing temperature, the muon spins depolarize faster, showing a considerably large nonrelaxing component down to 20 mK. This suggests the presence of a nonmagnetic volume fraction in the ground state. We detect no signature for static magnetism down to 20 mK, such as coherent oscillation signal, loss of the initial asymmetry, and 1/3 recovery in a long time, suggesting the dynamic nature of the magnetic ground state.

For quantitative analysis, we fit the ZF- and LF-μSR spectra with the sum of a simple exponential function and constant, $P_z(t) = P_z(0)[f\exp(-\lambda_{\mathrm{ZF/LF}}t) + (1 - f)]$, where $P_z(0)$ is the initial muon spin polarization at $t = 0$, λ_{ZF} (λ_{LF}) is the muon spin relaxation rate in ZF (LF), and f $(1 - f)$ is the (non)relaxing fraction. In fitting the LF data, we used the fixed value of f obtained from the ZF analysis at the respective temperature.

The temperature dependence of the muon relaxation rate is depicted in Fig. 4(b). Upon cooling from high temperature, $\lambda_{\mathrm{ZF}}(T)$ steeply increases and becomes temperature-independent below 30 K. This temperature is comparable to the temperature at which $\chi_{\mathrm{int}}(T)$ manifests the change of the Curie-Weiss behavior [Fig. 1(c)]. The observed thermal evolution of λ_{ZF} is reminiscent of a thermally activated process. Thus we fit the data using a phenomenological function, $\lambda_{\mathrm{ZF}}(T) = \lambda_{\mathrm{ZF}}(0)[1 - \exp(-\Delta/T)]$, where Δ is the activation energy and $\lambda_{\mathrm{ZF}}(0)$ is the low-T limit of the muon spin relaxation rate [35]. As plotted by the solid line in Fig. 4(b), $\lambda_{\mathrm{ZF}}(T)$ is well reproduced by the thermally activated

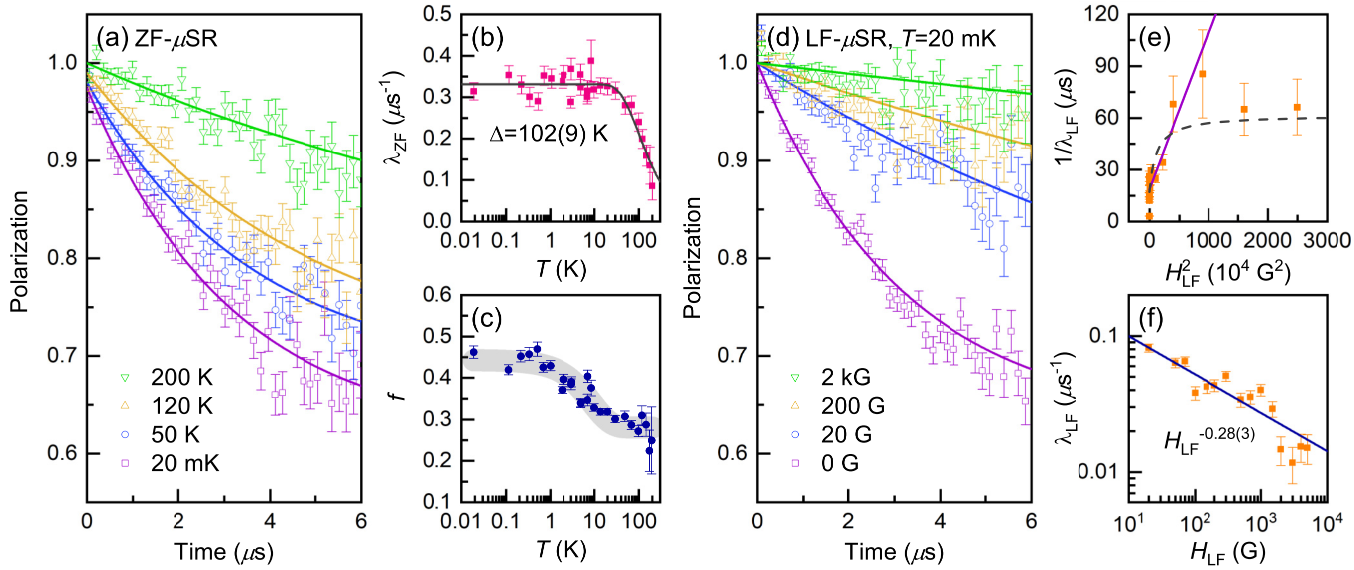

FIG. 4. (a) Representative ZF-μSR spectra at various temperatures together with the fitted curves. (b) Temperature dependence of the muon spin relaxation rate in a semilog scale. The solid line represents the fits using a phenomenological function for the Arrhenius-type thermally activated behavior. (c) Relaxing fraction f as a function of temperature. The shaded region is a guide to the eye. (d) LF dependence of the μSR spectra at $T = 20$ mK along with the fitting results. (e) $1/\lambda_{LF}$ vs. H^2_{LF}. The solid and dashed curves denote the fits using the Redfield formula with/without the field-independent consant λ^0_{LF}, respectively. (f) LF dependence of the muon spin relaxation rate in a log-log scale. The solid line indicates the power-law behavior of the muon spin relaxation rate.

exponential behavior with the fitting parameters of $\Delta = 102(9)$ K and $\lambda_{ZF}(0) = 0.331(5)\ \mu s^{-1}$. Apparently, there is no crystal-field excitation from the composite elements, Y^{3+} ($4d^0$)and Ti^{4+} ($3d^0$). Considering the dimer-based triangular lattice, $\lambda_{ZF}(T)$ should be ascribed to the singlet-triplet excitation of the Rh_2O_9 dimer. At high temperatures ($k_BT \gg \Delta$), the spins are in a rapidly fluctuating regime, giving rise to a tiny contribution to the muon spin relaxation. With decreasing temperature, thermal energy excites the singlet state to the excited state, leading to the increment of $\lambda_{ZF}(T)$. Lastly, at low temperatures, ($k_BT \ll \Delta$), the spin singlets are frozen out, resulting in the nearly temperature-independent relaxation rate. Nonetheless, in the case of the uniformly mixed-valence dimers $Rh^{4+}Rh^{3+}O_9$, the formation of a spin gap cannot be explained, naturally raising the possibility of different dimer configurations (see below).

In Fig. 4(c), we plot the relaxing fraction as a function of temperature. At high T, the relaxing fraction f is nearly temperature-independent with a value of $\sim$0.3. As the temperature is lowered, f tends to increase through 10 K and saturates to $\sim$0.45 below 1 K. $f(T)$ reflects the change of detectable magnetic volume fraction with lowering temperature in the system.

The thermal evolution of λ and f can be understood in terms of muon interstitial sites and Rh_2O_9 dimer configurations. In oxide materials, it is known that positive muons are preferably located near the apical oxygen of oxygen octahedra [36,37]. Therefore the implanted muons are likely to reside near the top and bottom of Rh_2O_9 dimer unit. Further, if we assume the randomly distributed Rh^{4+} and Rh^{3+}, three distinct dimer units are expected to be present, a magnetic $Rh_2^{4+}O_9$, nonmagnetic $Rh_2^{3+}O_9$, and orphan-spin-like $Rh^{4+}Rh^{3+}O_9$ [Fig. 1(d)]. When their population is identical, each unit would have a fraction of 1/3. At high T, $Rh_2^{4+}O_9$ with the predominant intradimer interaction governs spin dynamics with the singlet-triplet gap, leading to the detectable magnetic volume fraction of 1/3. Concurrently, the Rh^{4+} moment in $Rh^{4+}Rh^{3+}O_9$ dynamically fluctuates by thermal energy. However, as reported in valence bond glass systems, the relaxation by dangling spins is typically quite slow ($\sim$0.05 μs^{-1} at sub-Kelvin temperatures) [8,38], less likely to be discernible at high T. Upon cooling the temperature, the interdimer interactions become prominent at low temperatures. Consequently, the relaxing fraction of $Rh^{4+}Rh^{3+}O_9$ is discernible, giving rise to the additional magnetic volume fraction of $1/6(= 1/3 \times 1/2)$ at low T, but its relaxation is still negligible in the presence of the other dominant relaxation. In line with the proposed scenario, the relaxing fraction f has the value of $\sim$0.3 and $\sim$0.45, close to 1/3 and 1/2, at high and low temperatures, respectively.

We turn to the LF-μSR results. LF can decouple the muon spins from local fields at muon interstitial sites, providing information about internal field distribution and spin-spin correlations. Figure 4(d) shows the representative LF-μSR spectra at 20 mK in various LF. With the applied weak LF of 20 G, the muon spin polarization is considerably recovered by $\sim$20% at long times, suggesting the extremely weak internal fields developed at the muon interstitial sites. Upon further increasing LF, the polarization is monotonically recovered and nearly saturated in $H_{LF} = 2$ kG with small residual relaxation. The weak depolarization in 2 kG indicates the presence of small but finite dynamic magnetism.

For the exponentially decaying spin-spin correlations function $\mathcal{S}(t) \propto \exp(-\nu t)$, the LF dependence of the muon spin relaxation rate can be described by the Redfield formalism, $\lambda_{LF}(H_{LF}) = 2\gamma_\mu^2 H_{loc}^2 \nu/(\nu^2 + \gamma_\mu^2 H_{LF}^2) + \lambda^0_{LF}$, where γ_μ is the

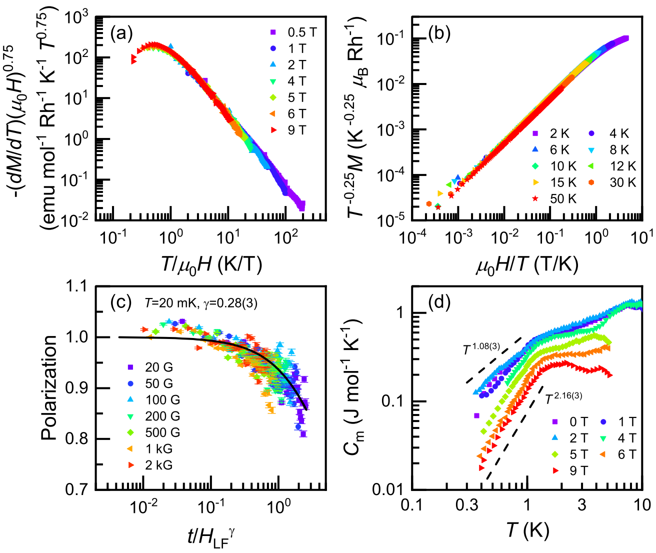

FIG. 5. (a) Scaling plot of the dc magnetic susceptibility, $-(dM/dT)B^{0.75}$ vs T/B. (b) $T-B$ scaling of the isothermal magnetization. (c) Time-field scaling plot of the muon spin polarization, $P_z(t)$ vs t/H^γ at 20 mK. The solid line is the scaled fitting curve at 20 mK in 20 G. (d) Magnetic specific heat at different applied fields in a log-log scale. The dashed lines indicate the power-law behavior $C_m(T) \sim T^\eta$.

muon gyromagnetic ratio, $H_{\rm loc}$ is the fluctuating field at the muon site, ν is the fluctuation frequency, and $\lambda^0_{\rm LF}$ is the field-independent relaxation rate. Such a correlation gives rise to the Lorentzian spectral density $\mathcal{S}(\omega)$ [39]. However, as depicted in Fig. 4(e), the Redfield formula provides a poor description of $\lambda_{\rm LF}(H_{\rm LF})$, intimating a nonexponentially decaying spin correlation function.

Alternatively, in the case of a power-law decaying exponential function $\mathcal{S}(t) \propto t^{-(1-\gamma)}$, the spectral density is given by $\mathcal{S}(\omega) \propto \omega^{-\gamma}$ [40]. As illustrated in Fig. 4(f), $\lambda_{\rm LF}(H_{\rm LF})$ follows the power-law dependence $\lambda_{\rm LF} \propto H_{\rm LF}^{-\gamma}$ with $\gamma = 0.28(3)$. The sublinear power-law behavior suggests the unconventional spin correlation function $\mathcal{S}(t) \propto t^{-0.72}$ and spectral density $\mathcal{S}(\omega) \propto \omega^{-0.28}$. Such algebraically decaying spin correlations are observed in various QSL materials with spin chain, pyrochlore, kagome, and triangular lattices [40–43]. The observed power-law spin correlation of $Ba_6Y_2Rh_2Ti_2O_{17-\delta}$ is comparable to that of the triangular QSL candidates $YbMgGaO_4$ and $RbAg_2Cr[VO_4]_2$ ($\gamma = 0.3-0.34$) [43,44] (see Appendix A for more details on the spin-spin correlation function).

C. Scaling behavior

As previously reported in Ref. [22], $Ba_6Y_2Rh_2Ti_2O_{17-\delta}$ exhibits the scaling behavior of the total specific heat, heralding the possibility of a QSL state. We attempt to verify the scaling relation in other physical quantities, $M(H,T)$ and $C_m(H,T)$ in H/T and $P_z(t)$ in $t/H_{\rm LF}$ (see Appendix B for the specific heat analysis). In Fig. 5(a), we present the scaling plot of $-(dM/dT)H^{\alpha_\chi}$ vs. T/μ_0H. The dc susceptibility data collapse onto a single curve with the exponent of $\alpha_\chi = 0.75$. The magnetization data scaled by temperature $MT^{1-\alpha_{\rm M}}$ overlap over a four-decade range of μ_0H/T with the exponent of $\alpha_{\rm M} = 0.75$ [Fig. 5(b)]. Furthermore, the muon spin polarization displays the time-field scaling behavior with the exponent $\alpha_\mu = 1-\gamma = 0.72$ at 20 mK as exhibited in Fig. 5(c). On the other hand, we find no scaling relation of the magnetic specific heat in T/H, inconsistent with the previous result that displays the scaling behavior of the total specific heat with the exponent $\alpha_{\rm C} = 0.5$ [22].

The breakdown of the scaling relation in $C_m(H,T)$ can be understood in terms of the structural orphan spin contribution. In a QSL and a valence bond with quenched disorder, the low-energy density of states follows the power-law distribution $D(E) \propto E^{-\alpha}$, yielding the power-law dependence of the physical quantities $\chi(T) \sim T^{-\alpha}$, $M(T) \sim H^{1-\alpha}$, and $C(T) \sim T^{1-\alpha}$ [9]. Our magnetic specific heat data present the power-law behavior $C_m(H,T) \sim T^\eta$ with $\eta = 1.08(3)$–$2.16(3)$, negating the scaling relation with $\alpha = 0.72$–0.75. Rather, the T-linear dependence in zero field is reminiscent of gapless excitations in QSLs [23–25,45,46] or random-singlet state [14]. In addition, $C_m(T)$ for $\mu_0H \geqslant 4$ T shows a power-law dependence T^η with $\eta \sim 2.16(2)$, close to the quadratic dependence observed in the weakly disordered frustrated magnets featuring the scaling relation [24]. In $Ba_6Y_2Rh_2Ti_2O_{17-\delta}$, the conventional orphan spins originating from the mixed Rh^{4+} and Rh^{3+} ions would affect the low-lying density of magnetic states, giving rise to the failure of the power-law scaling in the magnetic specific heat. Nevertheless, interestingly, $Ba_6Y_2Rh_2Ti_2O_{17-\delta}$ has characteristics in common with the QSLs with quenched disorder.

IV. DISCUSSION AND CONCLUSION

Combining magnetic, thermodynamic, and local-probe measurements, we reveal (i) the presence of structural orphan spins, (ii) the dynamic magnetic ground state, (iii) the thermally activated singlet-triplet excitation, and (iv) the scaling relation of the physical quantities arising from random magnetism. These observations suggest that the magnetic ground state is comprised of weakly interacting conventional orphan spins and dimer singlets.

Based on these findings, we discuss the spin dimer configurations of $Ba_6Y_2Rh_2Ti_2O_{17-\delta}$. We showcase the possible Rh arrangements as illustrated in Fig. 1 and consider their relevance to the studied compound. First, a uniform triangular lattice of $Rh^{4+}Rh^{3+}O_9$ [Fig. 1(a)] cannot explain magnetism composed of two different energy scales, the singlet-triplet gap and the conventional orphan spins, due to the lack of the singlet dimer $Rh_2^{4+}O_9$. Second, a distorted triangular layer [Fig. 1(b)] accounts for exchange randomness by coexisting J_1 and J_2, but not for the singlet-triplet excitation because the basic building block is $Rh^{4+}Rh^{3+}O_9$. Third, a dimer-based depleted triangular lattice [Fig. 1(c)] describes the gapped excitation and the competing interactions, but not for the structural orphan spins. Lastly, the randomly distributed Rh^{4+} and Rh^{3+} configuration [Fig. 1(d)] provides a rationale for our observations, including the singlet-triplet excitation, random magnetism with competing exchange interactions, and structural orphan spins. Nonetheless, the last model cannot explain the absence of a singlet-dimer signature in $\chi(T)$. Thus, it is fair to say that all the considered configurations can be mixed up even though some configurations occupy a more population than the others. The mixed configurations could give rise to the resemblance to the random-singlet state, signified by the scaling relations of the physical quantities.

To conclude, we have characterized the magnetic properties of the dimer-based triangular antiferromagnet $Ba_6Y_2Rh_2Ti_2O_{17-\delta}$ using the magnetic, thermodynamic, and local-probe techniques. We find weakly interacting structural orphan spins in the fluctuating singlet background. The magnetic ground state closely resembles random singlets, exhibiting scaling behaviors in our thermodynamic and dynamic quantities. This is attributed to the randomly arranged $Rh_2^{4+}O^9$, $Rh_2^{3+}O_9$, and $Rh^{4+}Rh^{3+}O_9$ dimers, originating from the nearly 1:1 mixed valence character of the Rh^{4+} and Rh^{3+} ions by oxygen deficiency. $Ba_6Y_2Rh_2Ti_2O_{17-\delta}$, thus, provides a prominent foundation for understanding the role of quenched disorder in cluster-based frustrated magnets.

ACKNOWLEDGMENTS

S.L. acknowledges support from the Institute for Basic Science (IBS-R014-Y2). The work at SKKU is supported by the National Research Foundation (NRF) of Korea (Grants No. 2022R1A2C1003959 and No. 2020R1A5A1016518). Work at Princeton University was supported by the Institute for Quantum Matter, an Energy Frontier Research Center funded by DOE, Office of Science, Basic Energy Sciences under Award DE-SC0019331.

APPENDIX A: LF-μSR

To further confirm the algebraic spin correlation in $Ba_6Y_2Rh_2Ti_2O_{17-\delta}$ in phenomenological level, we attempt to analyze the LF-μSR spectra at 20 mK with the theoretical muon spin relaxation function. For QSLs with the power-law spin correlation, it is proposed that the LF-μSR spectra can be expressed as [47]

$$P_z(t) = \exp[-\Psi_z(t)], \tag{A1}$$

where $\Psi_z(t) = (\Upsilon\xi t)^{2-x} K_x(\omega_\mu f t)$ with $\Upsilon^{2-x} = 2\gamma_\mu^2 \Delta^2 \tau_e^x$ and $K_x(z) = \frac{\sin(\pi x/2)\Gamma(1-x)}{\pi} \int_{-\infty}^{\infty} \frac{1-\cos y}{|y+z|^{1-x} y^2} dy$. Here, γ_μ is the muon gyromagnetic ratio, ω_μ is the muon precession frequency in H_{LF}, x is the exponent with the range of $0 < x < 1$, τ_e is the electronic correlation time, $\Gamma(x)$ is the gamma function, ξ is the fraction where the fields by singlets act at the muon site, and $1-\xi$ is the fraction where the fields are negligible.

As presented in Fig. 6, the ZF data exhibit a poor description by the theory because the initial decay of the muon spin polarization has an exponential shape rather than a Gaussian one. The deviation between the ZF data and the theory suggests the presence of nonalgebraic spin correlations. Nevertheless, the LF data in agreement with Eq. (A1), indicate the presence of algebraic spin correlations. Based on these observations, we deduce that the spin-spin correlation function has both the exponential and algebraic contributions simultaneously, $\mathcal{S}(t) \propto t^{-(1-\gamma)} \exp(-\nu t)$. Note that the obtained parameters in $H_{LF} > 0$ (Table II) are somewhat comparable with those of $ZnCu_3(OH)_6Cl_2$ [$x = 0.57(7)$, $\xi = 0.004(1)$, $(\Upsilon f)^{-1} = 35(5)\,\mu s$] [47].

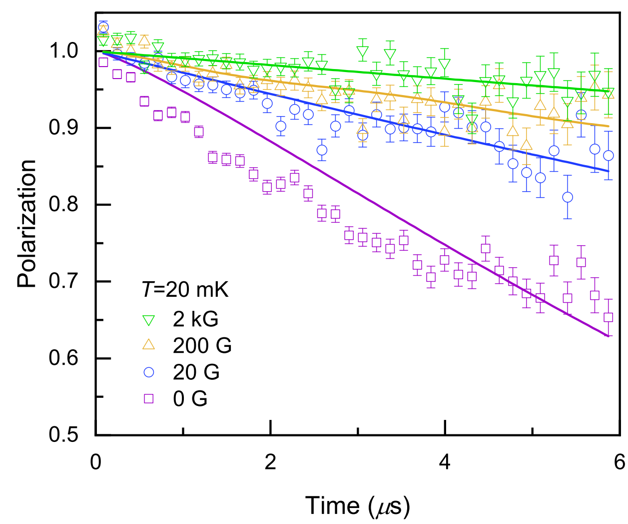

FIG. 6. LF dependence of μSR spectra at $T = 20$ mK. The solid curves are the fits using the Eq. (A1).

It should be noted that the imaginary part of the dynamical susceptibility is associated with the spectral density in the high-temperature limit, yielding the relation of $\mathrm{Im}\{\chi(\omega)\} \propto \omega^x$ [47]. Our analysis signifies that $\mathrm{Im}\{\chi(\omega)\} \propto \omega^x$ with $x = 0.56 - 0.78$ in the µeV energy scale [47]. In $ZnCu_3(OH)_6Cl_2$, defect spins are considered as a possible origin of $\mathrm{Im}\{\chi(\omega)\}$ in the µeV range because kagome spins show gapped magnetic excitations [47,48]. Similarly, in $Ba_6Y_2Rh_2Ti_2O_{17-\delta}$, the structural orphan spins possibly give rise to the power-law dependence of $\mathrm{Im}\{\chi(\omega)\}$ at extremely low energies.

APPENDIX B: SPECIFIC HEAT ANALYSIS

Figure 7(a) exhibits the temperature dependence of the raw specific heat divided by temperature. As pointed out in Ref. [22], the broad hump around 1 K in $C_p(T)/T$ is indicative of a Schottky anomaly. In order to estimate the magnetic specific heat $C_m(T)$, we decompose the total specific heat $C_p(T)$ into three contributions, $C_p = C_{np} + C_{lat} = C_m + C_{Sch} + C_{lat}$. Here, C_{np} is the nonphononic specific heat that is the sum of C_m and C_{Sch}, C_{lat} is the lattice specific heat, C_{Sch} is the Schottky anomaly arising from the structural orphan spins, and C_m is the magnetic specific heat.

By subtracting $C_{lat}(T)$ using the nonmagnetic counterpart $Ba_6Y_2Ti_4O_{17}$, we obtain $C_{np}(T)$ at different fields. To differentiate the Schottky contribution, we plot the difference between the 0 T and $\mu_0 H = 1, 2, 4$ T data, $\Delta C_{np}/T = [C_{np}(0\,T) - C_{np}(H)]/T$ in Fig. 7(b). It is well known that the field-dependent part of C_{np}/T can be modeled by the

TABLE II. Extracted fitting parameters using Eq. (A1).

H_{LF} (G)	x	ξ	$(\Upsilon\xi)^{-1}$ (µs)
0	0.7814	0.0357	32.6474
20	0.6579	0.0463	36.9334
200	0.5758	0.1043	21.0127
2000	0.5675	0.1025	15.5129

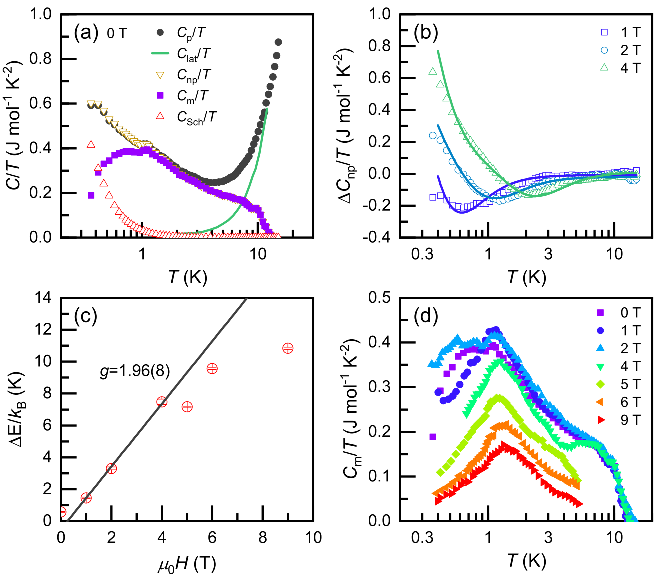

FIG. 7. (a) Temperature dependence of the specific heat divided by temperature. The total specific heat C_p is decomposed into the lattice C_{lat}, Schottky C_{Sch}, and magnetic C_m contributions. (b) $\Delta C_p/T = [C_p(0\,T) - C_p(H)]/T$. The solid curves are fits to the data as described in the text. (c) Field depdnence of the Schottky gap $\Delta E/k_B$. The solid line represents the fit to Zeeman splitting. (d) C_m/T vs T at different fields in a semilog scale.

uniformly distributed zero-field split doublets as observed in other frustrated magnets with $S = 1/2$ orphan spins [49,50]. As shown in Fig. 7(b), the Schottky contribution is well described with $\Delta C_{np}/T = n_{orp}R[C_{Sch}(\Delta E_{H_1}) - C_{Sch}(\Delta E_{H_2})]/T$. Here, n_{orp} is the orphan spin concentration, R is the Boltzmann constant, ΔE_{H_i} is the energy of two-level splitting by applied field H_i, and $C_{Sch}(\Delta E_{H_i}) = [\Delta E_{H_i}/k_B T]^2 \exp[-\Delta E_{H_i}/k_B T]$.

The best fit is obtained with the global fitting parameter of $\Delta E_{H_1=0\,T}/k_B = 0.57(2)$ K, yielding the orphan spin concentration of $n_{orp} = 6.6(3), 5.1(2), 11.3(5)\%$ for $\mu_0 H = 1, 2, 4$ T, respectively. The estimated n_{orp} is comparable to that from the isothermal magnetization in Table I. The obtained ΔE_H is depicted in Fig. 7(c). The linear fit to $\Delta E/k_B$ for $1 \leqslant \mu_0 H \leqslant 4$ T suggests the Zeeman splitting with $g = 1.96(8)$. Note that we also estimate the orphan spin contribution for the higher field data with the fixed value of $n_{orp}^{avg} = 7.6\%$. However, the lack of high-T data gives rise to uncertainty in the evaluation of ΔE, leading to the deviation from the linearity of $\Delta E/k_B$.

In Fig. 7(d), C_m/T at different fields are displayed. We find the broad maximum at $T \sim 1.3$ K for $\mu_0 H = 0 - 9$ T, which is robust with increasing fields. This temperature is comparable to the temperature where the relaxing fraction f levels off [Fig. 4(c)]. The observed broad maximum in C_m/T is possibly related to the development of the magnetic correlations between the localized and orphan moments.

[1] T. M. Rice, To condense or not to condense, Science **298**, 760 (2002).

[2] S. E. Sebastian, N. Harrison, C. D. Batista, L. Balicas, M. Jaime, P. A. Sharma, N. Kawashima, and I. R. Fisher, Dimensional reduction at a quantum critical point, Nature (London) **441**, 617 (2006).

[3] A. Furrer and O. Waldmann, Magnetic cluster excitations, Rev. Mod. Phys. **85**, 367 (2013).

[4] H. Kageyama, K. Yoshimura, R. Stern, N. V. Mushnikov, K. Onizuka, M. Kato, K. Kosuge, C. P. Slichter, T. Goto, and Y. Ueda, Exact dimer ground state and quantized magnetization plateaus in the two-dimensional spin system $SrCu_2(BO_3)_2$, Phys. Rev. Lett. **82**, 3168 (1999).

[5] P. G. Radaelli, Y. Horibe, M. J. Gutmann, H. Ishibashi, C. H. Chen, R. M. Ibberson, Y. Koyama, Y.-S. Hor, V. Kiryukhin, and S.-W. Cheong, Formation of isomorphic Ir^{3+} and Ir^{4+} octamers and spin dimerization in the spinel $CuIr_2S_4$, Nature (London) **416**, 155 (2002).

[6] P. W. Anderson, Resonating valence bonds: A new kind of insulator? Mater. Res. Bull. **8**, 153 (1973).

[7] L. Balents, Spin liquids in frustrated magnets, Nature (London) **464**, 199 (2010).

[8] M. A. de Vries, A. C. Mclaughlin, and J.-W. G. Bos, Valence bond glass on an fcc lattice in the double perovskite Ba_2YMoO_6, Phys. Rev. Lett. **104**, 177202 (2010).

[9] I. Kimchi, A. Nahum, and T. Senthil, Valence bonds in random quantum magnets: Theory and application to $YbMgGaO_4$, Phys. Rev. X **8**, 031028 (2018).

[10] K. Watanabe, H. Kawamura, H. Nakano, and T. Sakai, Quantum spin-liquid behavior in the spin-1/2 random Heisenberg antiferromagnet on the triangular lattice, J. Phys. Soc. Jpn. **83**, 034714 (2014).

[11] L. Savary and L. Balents, Disorder-induced quantum spin liquid in spin ice pyrochlores, Phys. Rev. Lett. **118**, 087203 (2017).

[12] L. Liu, H. Shao, Y.-C. Lin, W. Guo, and A. W. Sandvik, Random-singlet phase in disordered two-dimensional quantum magnets, Phys. Rev. X **8**, 041040 (2018).

[13] S. Sanyal, K. Damle, J. T. Chalker, and R. Moessner, Emergent moments and random singlet physics in a Majorana spin liquid, Phys. Rev. Lett. **127**, 127201 (2021).

[14] H. Kawamura and K. Uematsu, Nature of the randomness-induced quantum spin liquids in two dimensions, J. Phys.: Condens. Matter **31**, 504003 (2019).

[15] Z. Zhu, P. A. Maksimov, S. R. White, and A. L. Chernyshev, Disorder-induced mimicry of a spin liquid in $YbMgGaO_4$, Phys. Rev. Lett. **119**, 157201 (2017).

[16] A. Kitaev, Anyons in an exactly solved model and beyond, Ann. Phys. **321**, 2 (2006).

[17] J. Knolle, R. Moessner, and N. B. Perkins, Bond-disordered spin liquid and the honeycomb iridate $H_3LiIr_2O_6$: Abundant low-energy density of states from random Majorana hopping, Phys. Rev. Lett. **122**, 047202 (2019).

[18] W.-H. Kao, J. Knolle, G. B. Halász, R. Moessner, and N. B. Perkins, Vacancy-induced low-energy density of states in the Kitaev spin liquid, Phys. Rev. X **11**, 011034 (2021).

[19] C. Lee, S. Lee, Y. Choi, C. Wang, H. Luetkens, T. Shiroka, Z. Jang, Y.-G. Yoon, and K.-Y. Choi, Coexistence of random singlets and disordered Kitaev spin liquid in $H_3LiIr_2O_6$, Phys. Rev. B **107**, 014424 (2023).

[20] O. Mustonen, S. Vasala, E. Sadrollahi, K. P. Schmidt, C. Baines, H. C. Walker, I. Terasaki, F. J. Litterst, E. Baggio-Saitovitch,

and M. Karppinen, Spin-liquid-like state in a spin-1/2 square-lattice antiferromagnet perovskite induced by $d^{10}-d^{0}$ cation mixing, Nat. Commun. **9**, 1085 (2018).

[21] S. Yoon, W. Lee, S. Lee, J. Park, C. H. Lee, Y. S. Choi, S.-H. Do, W.-J. Choi, W.-T. Chen, F. Chou, D. I. Gorbunov, Y. Oshima, A. Ali, Y. Singh, A. Berlie, I. Watanabe, and K.-Y. Choi, Quantum disordered state in the J_1-J_2 square-lattice antiferromagnet $Sr_2Cu(Te_{0.95}W_{0.05})O_6$, Phys. Rev. Mater. **5**, 014411 (2021).

[22] L. T. Nguyen, D. B. Straus, Q. Zhang, and R. J. Cava, Widely spaced planes of magnetic dimers in the $Ba_6Y_2Rh_2Ti_2O_{17-\delta}$ hexagonal perovskite, Phys. Rev. Mater. **5**, 034419 (2021).

[23] K. Kitagawa, T. Takayama, Y. Matsumoto, A. Kato, R. Takano, Y. Kishimoto, S. Bette, R. Dinnebier, G. Jackeli, and H. Takagi, A spin-orbital-entangled quantum liquid on a honeycomb lattice, Nature (London) **554**, 341 (2018).

[24] I. Kimchi, J. P. Sheckelton, T. M. McQueen, and P. A. Lee, Scaling and data collapse from local moments in frustrated disordered quantum spin systems, Nat. Commun. **9**, 4367 (2018).

[25] J. S. Helton, K. Matan, M. P. Shores, E. A. Nytko, B. M. Bartlett, Y. Yoshida, Y. Takano, A. Suslov, Y. Qiu, J. H. Chung, D. G. Nocera, and Y. S. Lee, Spin dynamics of the spin-1/2 kagome lattice antiferromagnet $ZnCu_3(OH)_6Cl_2$, Phys. Rev. Lett. **98**, 107204 (2007).

[26] A. Suter and B. M. Wojek, Musrfit: A free platform-independent framework for μSR data analysis, Phys. Procedia **30**, 69 (2012).

[27] S. K. Ma, C. Dasgupta, and C. K. Hu, Random antiferromagnetic chain, Phys. Rev. Lett. **43**, 1434 (1979).

[28] J. E. Hirsch and J. V. Jose, Singular thermodynamic properties in random magnetic chains, Phys. Rev. B **22**, 5339 (1980).

[29] A. H. Castro Neto, G. Castilla, and B. A. Jones, Non-Fermi liquid behavior and griffiths phase in f-electron compounds, Phys. Rev. Lett. **81**, 3531 (1998).

[30] S. Yoon, C. H. Lee, S. Lee, Y. S. Choi, S.-H. Do, M. Abdel-Jawad, I. Watanabe, B. J. Suh, and K.-Y. Choi, Spin dynamics in the staircase kagome lattice compound $PbCu_3TeO_7$, Phys. Rev. B **98**, 214401 (2018).

[31] K. W. Blazey and F. Levy, EPR of rhodium, osmium and iridium-doped rutile, Solid State Commun. **59**, 335 (1986).

[32] E. Janod, C. Payen, F.-X. Lannuzel, and K. Schoumacker, Random interactions and spin-glass thermodynamic transition in the hole-doped Haldane system $Y_{2-x}Ca_xBaNiO_5$, Phys. Rev. B **63**, 212406 (2001).

[33] K.-Y. Choi, P. Lemmens, J. Pommer, A. Ionescu, G. Guntherodt, S. Hiroya, H. Sakurai, K. Yoshimura, A. Matsuo, and K. Kindo, Random magnetism in the frustrated triangular spin ladder $KCu_5V_3O_{13}$, Phys. Rev. B **70**, 174417 (2004).

[34] S.-H. Do, J. van Tol, H. D. Zhou, and K.-Y. Choi, Dynamical spin-orbital correlations versus random singlets in $Ba_3CuSb_2O_9$ investigated by magnetization and electron spin resonance, Phys. Rev. B **90**, 104426 (2014).

[35] P. J. Baker, S. J. Blundell, F. L. Pratt, T. Lancaster, M. L. Brooks, W. Hayes, M. Isobe, Y. Ueda, M. Hoinkis, M. Sing, M. Klemm, S. Horn, and R. Claessen, Muon-spin relaxation measurements on the dimerized spin-1/2 chains $NaTiSi_2O_6$ and TiOCl, Phys. Rev. B **75**, 094404 (2007).

[36] S. R. Dunsiger, A. A. Aczel, C. Arguello, H. Dabkowska, A. Dabkowski, M.-H. Du, T. Goko, B. Javanparast, T. Lin, F. L. Ning, H. M. L. Noad, D. J. Singh, T. J. Williams, Y. J. Uemura, M. J. P. Gingras, and G. M. Luke, Spin ice: Magnetic excitations without monopole signatures using muon spin rotation, Phys. Rev. Lett. **107**, 207207 (2011).

[37] E. Holzschuh, A. B. Denison, W. Kundig, P. F. Meier, and B. D. Patterson, Muon-spin-rotation experiments in orthoferrites, Phys. Rev. B **27**, 5294 (1983).

[38] S. Lee, Wonjun Lee, W. Guohua, J. Ma, H. Zhou, M. Lee, E. S. Choi, and K.-Y. Choi, Experimental evidence for a valence-bond glass in the $5d^1$ double perovskite Ba_2YWO_6, Phys. Rev. B **103**, 224430 (2021).

[39] R. S. Hayano, Y. J. Uemura, J. Imazato, N. Nishida, T. Yamazaki, and R. Kubo, Zero-and low-field spin relaxation studied by positive muons, Phys. Rev. B **20**, 850 (1979).

[40] F. L. Pratt, S. J. Blundell, T. Lancaster, C. Baines, and S. Takagi, Low-temperature spin diffusion in a highly ideal $S=\frac{1}{2}$ Heisenberg antiferromagnetic chain studied by muon spin relaxation, Phys. Rev. Lett. **96**, 247203 (2006).

[41] A. Keren, J. S. Gardner, G. Ehlers, A. Fukaya, E. Segal, and Y. J. Uemura, Dynamic properties of a diluted pyrochlore cooperative paramagnet $(Tb_pY_{1-p})_2Ti_2O_7$, Phys. Rev. Lett. **92**, 107204 (2004).

[42] E. Kermarrec, A. Zorko, F. Bert, R. H. Colman, B. Koteswararao, F. Bouquet, P. Bonville, A. Hillier, A. Amato, J. van Tol, A. Ozarowski, A. S. Wills, and P. Mendels, Spin dynamics and disorder effects in the $S=\frac{1}{2}$ kagome Heisenberg spin-liquid phase of kapellasite, Phys. Rev. B **90**, 205103 (2014).

[43] S. Lee, R. Klauer, J. Menten, W. Lee, S. Yoon, H. Luetkens, P. Lemmens, A. Möller, and K.-Y. Choi, Unconventional spin excitations in the $S=\frac{3}{2}$ triangular antiferromagnet $RbAg_2Cr[VO_4]_2$, Phys. Rev. B **101**, 224420 (2020).

[44] Y. Li, D. Adroja, P. K. Biswas, P. J. Baker, Q. Zhang, J. Liu, A. A. Tsirlin, P. Gegenwart, and Q. Zhang, Muon spin relaxation evidence for the U(1) quantum spin-liquid ground state in the triangular antiferromagnet $YbMgGaO_4$, Phys. Rev. Lett. **117**, 097201 (2016).

[45] Y. S. Choi, C. H. Lee, S. Lee, S. Yoon, W.-J. Lee, J. Park, A. Ali, Y. Singh, J.-C. Orain, G. Kim, J.-S. Rhyee, W.-T. Chen, F. Chou, and K.-Y. Choi, Exotic low-energy excitations emergent in the random Kitaev magnet Cu_2IrO_3, Phys. Rev. Lett. **122**, 167202 (2019).

[46] Y. Li, B. Pan, S. Li, W. Tong, L. Ling, Z. Yang, J. Wang, Z. Chen, Z. Wu, and Q. Zhang, Gapless quantum spin liquid in the $S=1/2$ anisotropic kagome antiferromagnet $ZnCu_3(OH)_6SO_4$, New J. Phys. **16**, 093011 (2014).

[47] P. Dalmas de Réotier and A. Yaouanc, Power-law dynamics in the spin-liquid kagome lattices $SrCr_8Ga_4O_{19}$ and $ZnCu_3(OH)_6Cl_2$, Phys. Rev. B **105**, L241104 (2022).

[48] T.-H. Han, M. R. Norman, J.-J. Wen, J. A. Rodriguez-Rivera, J. S. Helton, C. Broholm, and Y. S. Lee, Correlated impuritiesand intrinsic spin-liquid physics in the kagome material herbertsmithite, Phys. Rev. B **94**, 060409(R) (2016).

[49] M. A. de Vries, K. V. Kamenev, W. A. Kockelmann, J. Sanchez-Benitez, and A. Harrison, Magnetic ground state of an experimental $S=1/2$ kagome antiferromagnet, Phys. Rev. Lett. **100**, 157205 (2008).

[50] H. D. Zhou, E. S. Choi, G. Li, L. Balicas, C. R. Wiebe, Y. Qiu, J. R. D. Copley, and J. S. Gardner, Spin liquid state in the $S=1/2$ triangular lattice $Ba_3CuSb_2O_9$, Phys. Rev. Lett. **106**, 147204 (2011).